Theoretical investigation of phase transitions in the shape memory alloy NiTi

Zhigang Wu [*] and John W. Lawson[†]

Intelligent Systems Division, NASA Ames Research Center, Moffett Field, California 94035, USA

There remain a few unsolved problems when the *ab initio* approach was applied to study one of the most important binary shape memory alloys (SMAs), NiTi (nitinol), which is the starting material for alloying numerous multicomponent SMAs. This hinders the computational design of complex SMAs with desirable properties. In this Letter we report that including the electronic free energy in the Gibbs free energy nearly reduces by half the large errors in previously predicted martensitic transition temperatures, and the controversy on the ground state of NiTi is resolved by reaching the convergence in free-energy calculations. In addition, the present results demonstrate that the martensitic transition path in stoichiometric NiTi is directly from B2 to B19′ without intermediate phases.

Introduction. Shape memory alloys (SMAs) recover their original shapes upon heating [1–3] due to the existence of a reversible martensitic transition (MT) between the high-temperature austenite (A) and low-temperature martensite (M) phases. The martensitic transition temperature (MTT), normally obtained by $(M_s + A_f)/2$ where M_s and A_f are the martensite start and austenite finish temperatures, respectively, is a crucial characteristic of an SMA, determining its operation temperature. SMAs have a wide range of potential applications in aerospace, civil engineering, bioengineering, etc. [1–7], but their operating temperatures are limited by the available SMAs. MTT can be tuned by alloying a binary with other metals, and the multicomponent NiTi-based SMAs have attracted tremendous research efforts lately [7–14]. It is not efficient to employ the trial-and-error method alone due to the drastically increased complexity and possibilities in compositions. Thus reliable theory and accurate computations [15–26] play an indispensable role in creating SMAs with desirable properties.

However, accurately predicting MTTs and other associated properties of SMAs from first principles remains a formidable task. Theoretically, MTT is defined as the temperature when the M and the A phases have the same Gibbs free energy (G). One needs to evaluate G of each phase of these materials within ~ 1 meV/atom, which is computationally very demanding due to the strong anharmonicity and mechanical instability in the austenite phase [21,22].

Furthermore, even for the prototype NiTi (nitinol), the simplest binary and probably most well known and most commonly used SMA [27], there still exist a number of unsolved problems when comparing theoretical results with measured data. In particular, the MTT of NiTi, corresponding to the transition between austenite B2 (cubic $Pm\bar{3}m$) and martensite B19′ (monoclinic $P2_1/m$, with a monoclinic angle

$\gamma \approx 98°$ [28,29]), was predicted to be in the range of 482–500 K using the state-of-the-art thermodynamics integration (TI) based on *ab initio* molecular dynamics (AIMD) simulations [21–23], compared with the measured MTT using the differential scanning calorimetry analysis, which is averaged to be 345 K, in a range of 334–358 K [30–32].[1] It is unclear if this large discrepancy is caused mainly by the single-crystal model used in first-principles calculations, while a realistic SMA always has defects and precipitates, etc., which might modify MTT substantially. If so, the microstructures and much larger unit cells are needed.

A long-standing controversy, however, is whether the zero-temperature ground state of NiTi is B19′ or B33 (orthorhombic *Cmcm*), which was theoretically predicted in the seminal publication by Huang *et al.* [15] but experimentally never discovered. Since the multiple paths from B2 to B33 prevent B33 from storing shape memory, extensive theoretical investigations have been carried out to settle this puzzle. Haskins *et al.* [21–23] predicted a B19′ → B33 transition at 75–83 K using TI, while Kumar and Waghmare determined it to be 49 K [26]. All previous studies conclude that at sufficiently low temperature, B33 is the most stable phase, and they suggest that either residual internal stress [15] or a small energy barrier [19,24] prevents the B19′ → B33 transition.

Finally, depending on the composition, NiTi-based alloys can go through different MT paths, which might involve the B19 (orthorhombic *Pmma*) or the R (rhombohedral $P3$ [35,36]) phase, e.g., the B2 → B19 → B19′ transition was found in ternary $Ti_{0.495}Ni_{0.455}Cu_{0.05}$ [9] and quaternary $Ti_{0.50}Ni_{0.44}Cu_{0.05}Al_{0.01}$ [8], the B2 → R → B19′ transition

---

*zhigang.wu@nasa.gov
†john.w.lawson@nasa.gov

---

[1]Previous publications [21–23] cited MTTs of NiTi in a range of 280–341 K [4,9,33,34]. But these data were not measured from the (nearly) equiatomic NiTi. MTT is sensitive to the NiTi composition, e.g., changing Ni from 50% to 51% results in a remarkable decrease of M_s by more than 100 K [5,33].

in Ni_4Ti_3 [37] (the appearance of R often depends on microstructures such as small grains, thin film surfaces, etc.), while the direct B2 → B19′ transition occurs in NiTi. This crucial characteristic has not been quantitatively studied from first principles.

In this Letter, we report on our recent theoretical exploration of phase transitions in NiTi. Employing the most accurate free-energy calculations we find that the error in the predicted MTT is reduced from 142 to 77 K, and the ground state of NiTi at 0 K is monoclinic B19′ ($\gamma \approx 101°$), compared with $\gamma \approx 98°$ just below MTT. The monoclinic angle increases with decreasing temperature and no monoclinic → orthorhombic transition occurs at low temperature. Our results also confirm a direct MT between B2 and B19′ without going through either the B19 or R phase for defect-free single crystals.

Methodologies. The Gibbs free energies of NiTi in various phases were evaluated from the following expression:

$$G(T) = E[V(T)] + F^{el}(T) + F_h^{ph}(T) + F_{anh}^{ph}(T). \quad (1)$$

Here, E is the total electronic energy for the reference structure, whose volume (V) is optimized at temperature T. $F^{el}(T)$ is the electronic free energy given by

$$F^{el}(T) = U^{el}(T) - TS^{el}(T). \quad (2)$$

We followed Ref. [38] to compute the electronic internal energy $U^{el}(T)$ and the configurational entropy $S^{el}(T)$, using the self-consistent approach and ten uncorrelated MD snapshots (see the convergence test in Table S1 in the Supplemental Material [39].) at each temperature considered.

$F_h^{ph}(T)$ is the harmonic part of the phonon free energy, and the anharmonic part of the phonon free energy, $F_{anh}^{ph}(T)$, is obtained using TI:

$$F_{anh}^{ph}(T) = \int_0^1 \left\langle \frac{\partial U}{\partial \lambda} \right\rangle_\lambda d\lambda. \quad (3)$$

Here, the potential energy U is given by

$$U(\lambda) = (1 - \lambda)U^h + \lambda U^{DFT}, \quad (4)$$

where the harmonic potential energy U^h is computed from the force constants of the reference structure, which are also used to calculate $F_h^{ph}(T)$ and $F_{anh}^{ph}(T)$. U^{DFT} is computed from the density functional theory (DFT) implemented in the VASP package [40–43], while the thermodynamic average $\langle \frac{\partial U}{\partial \lambda} \rangle$ for a fixed λ is obtained from the NVT AIMD simulations with the mixed potential $U(\lambda)$ for 10 ps, to ensure the error bar of F_{anh}^{ph} is less than 0.1 meV/atom. $\lambda = 0.0, 0.25, 0.50, 0.75, 1.0$ are used for integration in Eq. (3); the time step is 2.0 fs, and the friction factor for the Langevin thermostat is 100 fs.

We employed the upsampled thermodynamic integration using Langevin dynamics (UP-TILD [44]) approach to evaluate F_{anh}^{ph}. Specifically, AIMD simulations were performed with an energy cutoff (E_{cut}) of 300 eV and ∼3500 **k** points per reciprocal atom (KPPRA, i.e., the multiplication of the number of **k** points used in reciprocal space and the number of atoms in a unit cell in real space), while the upsampling of $\Delta U^{DFT} = U_{high}^{DFT} - U_{low}^{DFT}$ was done with $E_{cut} = 450$ eV and ∼27 000 KPPRA, which were also used for total energy and lattice dynamics calculations to ensure convergence. A more

detailed description of the computational procedures of obtaining G is in the Supplemental Material [39].

The PBE (parametrized by Perdew, Burke, and Ernzerhof [45]) density functional and the projector augmented-wave method (PAW [46,47]) were used in DFT calculations. The valence of Ni and Ti atoms include $3d^9 4s^1$ and $3d^2 4s^2$ electrons, respectively.

Martensitic transition. To determine the phase transition sequence and the MTT, we first optimized the structures of the B2, B19′ (note: if the γ angle is not specified, then it is 98°), B33, B19, and R phases. The optimized structural parameters and energetics of these phases are listed in Tables S2–S6 in the Supplemental Material [39], while Table S7 compares the present values of $E - E_{B2}$ with the previously calculated results using different methods.

Figure 1 summarizes the computed phonon distributions at 0 K for these five phases [blue lines in Figs. 1(a)–1(e)]. At 0 K, the B2, B19, and R phases are unstable, as indicated by imaginary (shown as negative frequency) phonons, while the B19′ and B33 are stable against lattice vibration. All other phases can be derived from the simplest B2 phase. The B19 phase is derived from B2 through an unstable phonon mode at the M point (1/2, 1/2, 0), while the R phase can be obtained from the transverse acoustic (TA) mode at (1/3, 1/3, 1/3) [17,18,36,49]. The slightly unstable TA branch along the $\Gamma \to Y$ direction in B19 leads to the monoclinic structure, and the orthorhombic B33 phase can be regarded as a special case of the monoclinic structure with $\gamma = 107.24°$.

The B2, R, and B19 phases can be entropically stabilized at higher temperatures, as demonstrated by their phonon distributions (red solid lines) at 400 K in Figs. 1(a)–1(c), respectively, and their phonon density of states (DOS) in Fig. 1(f), employing the temperature-dependent effective potential (TDEP [50,51]) method. Using the force constants of B2, R, and B19 phases at 400 K and B19′ at 0 K for 144-atom supercells, we evaluated $F_h^{ph}(T)$ and $F_{anh}^{ph}(T)$ at $T = 200, 300, 400, 500, 600$ K, and the differences in G for the B2, R, and B19 phases relative to the B19′ phase are plotted in Fig. 2. As illustrated by the dashed and solid black lines in Fig. 2, including the previously omitted electronic free energy F^{el} reduces ΔG between B2 and B19′, resulting in a decreased MTT from 487 to 422 K, much closer to the experimentally averaged value of 345 K.

The reduction in ΔG between B2 and B19′ is due to the fact that the magnitude of F^{el} (negative at finite temperature) of B2 is larger than that of B19′. Since the Fermi temperature of a metal is normally in the order of 10^4 K, the redistribution of electrons at a few hundred K relative to that at 0 K occurs mainly near the Fermi energy (E_{Fermi}), and the resulting U^{el} and S^{el} usually have larger magnitudes if the electronic DOS at E_{Fermi} is larger. As indicated in Fig. 3, the electronic DOS at E_{Fermi} of B2 is nearly twice as large as that of B19′ at 0 K, though the difference is slightly reduced at 400 K.

To check convergence, we carried out phonon free-energy calculations for B2 and B19′ at 600 K using larger and smaller supercells. As summarized in Table I, F^{ph} reaches a sufficient level of convergence (<1 meV/atom) using 144-atom supercells for NiTi. For both phases, though F_h^{ph} and F_{anh}^{ph} vary with the supercell size substantially due to the large variations in the calculated FCs, the variation in F^{ph}, the total
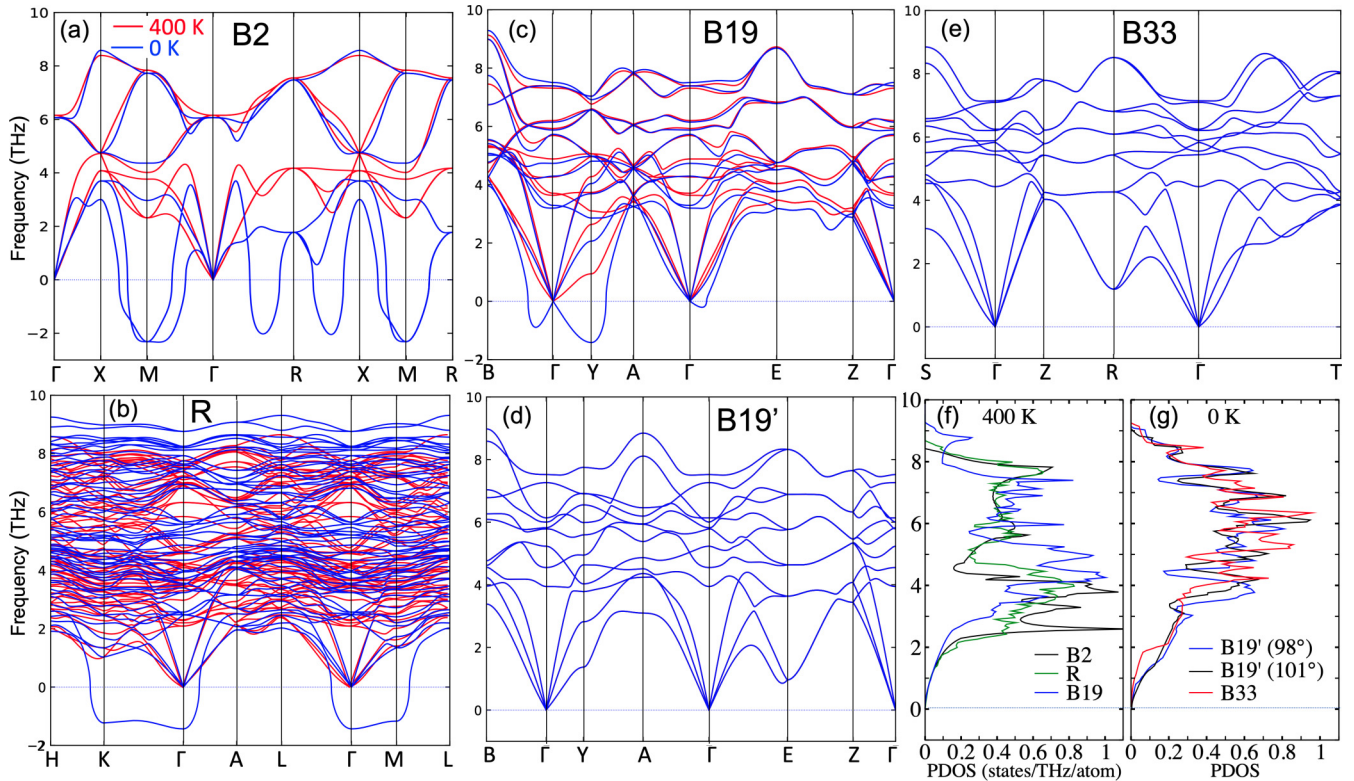
FIG. 1. Phonon dispersions (plotted using the PHONOPY program [48]) of the (a) B2, (b) R, (c) B19, (d) B19′ (98°), and (e) B33 phases at 0 K (blue lines) and 400 K (red lines). TDEP phonons are extrapolated from AIMD simulations using 128-atom supercells for B2 and 144-atom for R and B19, while 0 K phonons are calculated using 432-atom supercells for B2, 216-atom for R, and 384-atom for B19, B19′, and B33. Phonon density of states (PDOS) are plotted in (f) for B2, R, and B19 at 400 K and in (g) for B19′ (monoclinic angle $\gamma = 98°$ and 101°) and B33 at 0 K.

phonon free energy, is much smaller, especially for the stable (at 0 K) phase B19′, F^{ph}(48-atom, 600 K) $-F^{ph}$(144-atom, 600 K) is merely 0.8 meV/atom, while F^{ph}(48-atom, 600 K) $-F^{ph}$(144-atom, 600 K) = 2.3 meV/atom for the unstable (at

0 K) B2. In fact, MTT computed using the 48-atom supercells is 449 K, only 27 K higher than the converged value.

The data in the last row of Table I also demonstrate that for the stable phase B19′, the quasiharmonic approximation (QHA) is valid, i.e., F_{anh}^{ph} is negligible (<1 meV/atom), provided that the supercell is sufficiently large (∼400 atoms) and
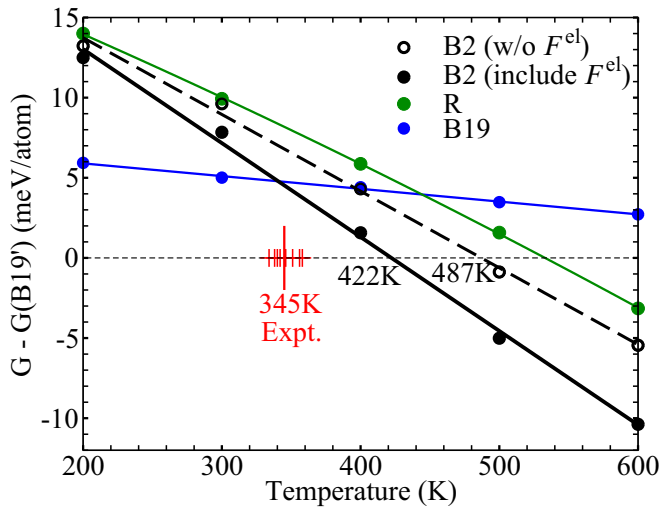
FIG. 2. Differences in Gibbs free energy G for B2 (black), R (green), and B19 (blue) phases relative to the B19′ phase. The open and solid black circles correspond to the calculated ΔG between B2 and B19′ omitting and including the electronic free energy F^{el}, respectively.
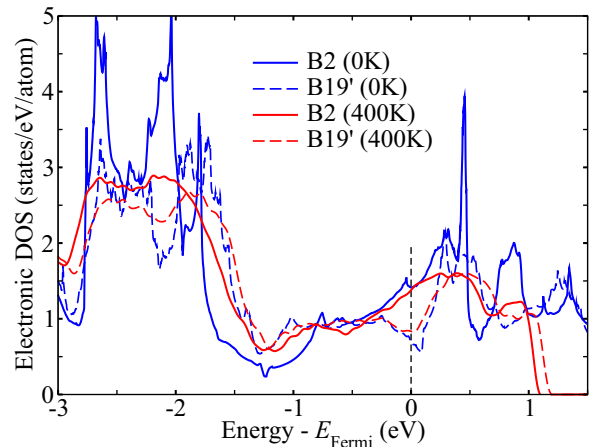
FIG. 3. Electronic density of states (DOS) for B2 (solid lines) and B19′ (dashed lines) at 0 K (blue) and 400 K (red). The electronic DOS at 400 K are the averaged DOS from ten uncorrelated snapshots in molecular dynamics simulations.

TABLE I. Calculated harmonic part ($F_{\mathrm{h}}^{\mathrm{ph}}$) and anharmonic part ($F_{\mathrm{anh}}^{\mathrm{ph}}$) of the phonon free energy in meV/atom, for B2 and B19′ phases at 600 K. The total phonon energy $F^{\mathrm{ph}} = F_{\mathrm{h}}^{\mathrm{ph}} + F_{\mathrm{anh}}^{\mathrm{ph}}$. N is the number of atoms in the supercell used. Here, the force constants (FCs) of B2 are TDEP results at 400 K, and FCs of B19′ are calculated for the structure optimized at 600 K, for comparison of QHA and TI.

	N	$F_{\mathrm{h}}^{\mathrm{ph}}$	$F_{\mathrm{anh}}^{\mathrm{ph}}$	F^{ph}
B2	48	−155.3	−37.6	−192.9
B2	144	−150.7	−45.1	−195.8
B2	432	−172.2	−23.0	−195.2
B19′	48	−133.2	−14.2	−147.4
B19′	144	−134.3	−14.2	−148.5
B19′	384	−148.0	−0.16	−148.2

the temperature is well below the melting point. In contrast, in the austenite phase, $F_{\mathrm{anh}}^{\mathrm{ph}}$ cannot be neglected even using very large supercells, since its anharmonicity is strong due to the presence of many imaginary phonon modes at 0 K [Fig. 1(a)].

Figure 2 also shows that the transition temperatures for R → B19′ and B19 → B19′ are well above that for B2 → B19′. Though below 340 K B19 has a lower G than B2, they both have higher G than B19′. Therefore, our calculations clearly demonstrate that neither R nor B19 is an intermediate phase for single-crystal NiTi, in which the MT is from B2 to B19′ directly.
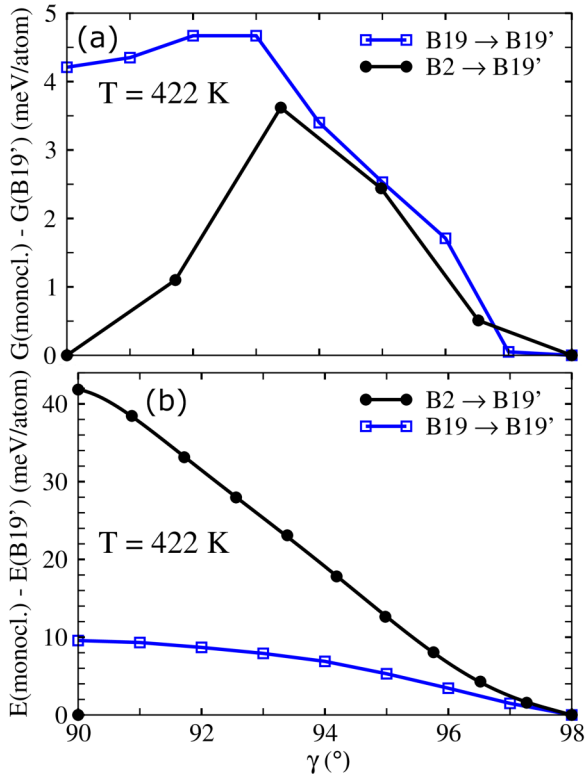
FIG. 4. (a) Gibbs free energy G and (b) energy E relative to those of the B19′ phase along B19 → B19′ (blue) and B2 → B19′ (black) transition paths.
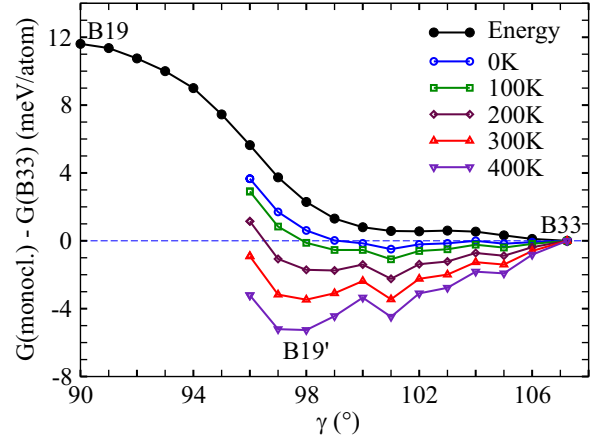
FIG. 5. Total energy (black) and the Gibbs free energy G of the monoclinic structure as functions of the monoclinic angle γ at various temperatures. Here, B19 is the energy maximum at $\gamma = 90°$, while B33 is the energy minimum at $\gamma = 107.24°$.

Figure 4(a) plots ΔG along the approximated transition path B2 → B19′ at the MTT, in comparison with ΔG along B19 → B19′. Here, the B2 → B19′ path was estimated by interpolation between these two phases, while B19 → B19′ was obtained by relaxing the monoclinic structures with fixed γ angles; therefore, B19 → B19′ is the minimum-energy path [Fig. 4(b)], whereas B2 → B19′ shall be the minimum-free-energy path, provided that the B2 → B19′ path is exact. When $\gamma < 94°$, ΔG along B2 → B19′ is significantly smaller than that along B19 → B19′, and the difference in ΔG [Fig. 4(a)] along these two paths becomes negligible when $\gamma > 94°$, though the difference in ΔE [Fig. 4(b)] is still significant.

The Landau-Falk theory of MT in SMAs [52] predicts a free-energy barrier (G_{b}) between the metastable austenite and martensite phases at MTT, when these two phases have the same value of G. We find that in NiTi, $G_{\mathrm{b}}(\mathrm{MTT}) \leqslant 3.6$ meV/atom, i.e., here, the computed value of 3.6 meV/atom is an upper limit of G_{b} at MTT, since the interpolated path was not obtained by optimizing G at each considered angle γ. Because of the existence of G_{b}, the martensitic transition does not start at MTT; instead, B2 → B19′ begins at a lower temperature, M_{s}, when ΔG can provide enough driving force to overcome the extra energies associated with nucleation. This is the origin of hysteresis in SMAs.

Low-temperature structures. Next, we discuss the structures and phase transitions at low temperatures, where B19 has a lower G than B2. Starting from B19 ($\gamma = 90°$), shear stress relaxation along ⟨011⟩ leads to a barrierless path from B19 to B33, which is the energy minimum at $\gamma = 107.24°$, as plotted in the black curve in Fig. 5. This is the main discovery by Huang *et al.* [15]. If B33 is the ground state and there is no energy barrier from B19′ to B33, why does the martensitic transition in NiTi occur between B2 and B19′ instead of between B2 and B33? Why is B19′ stabilized at this particular γ angle around 98° right after the martensite transition?

This is because though B33 is the energy minimum, B19′ (98°) is the minimum of the Gibbs free energy near MTT, as indicated by the purple curve in Fig. 5. When T further

decreases, the value of γ of the monoclinic structure with the lowest G increases; at 0 K, $\gamma \approx 101°$, i.e., B19′ (101°) is the true ground state and $G(B19′, 0\ K) - G(B33, 0\ K) = -0.49$ meV/atom. As shown in Fig. 1(g), most of the corresponding phonons tend to have slightly higher frequencies in B33 than in B19′, and thus the zero-point energy (ZPE) of B33 is higher than that of B19′. The difference in ZPE between B33 and B19′ (101°) is about 0.5 meV/atom larger than ΔE. At 0 K, as γ increases from 98° to 107.24°, both the energy difference (ΔE) and ZPE difference (ΔZPE) between B19′ and B33 are decreasing; however, around 101°, $\Delta E + \Delta ZPE$ reaches the minimum.

We note that for $T \gtrsim 50$ K, the TI (144-atom supercells) results and the QHA (384-atom supercells) results of the total phonon free energy are almost identical, and both TI and QHA approaches predict that G of B33 is lower than that of B19′ (98°) below 90 K, in agreement with previous findings [21–23]. However, as T is further decreased, TI becomes less applicable since TI is based on classical dynamics, which cannot well describe the low-temperature quantum dynamics.

Conclusions. In conclusion, the martensitic transition and the low-temperature phases in NiTi can be accurately predicted from the most advanced first-principles free-energy calculations using the perfect single-crystal structures, thus the computational design of multicomponent SMAs for improving properties from *ab initio* calculations becomes feasible. The zero-temperature ground state of NiTi is not the previously predicted B33; instead, it is B19′ with a slightly larger monoclinic angle than that just below the MT; thus even at very low temperature the memory is stored. Although in experiment certain levels of disorder, defects, and off-stoichiometricity always exist, we find that their effects on modifying MTT is by $\lesssim 100$ K (the error of the predicted MTT of NiTi is the largest among our calculated binary SMAs), which meets the minimum requirement for computationally designing SMAs with a designated working temperature range. Fundamentally, the single-crystal model of SMAs can be used to reveal the physical mechanisms driving the martensitic transition, which are still not clear and currently under active investigation by our research group.

[1] K. Otsuka and T. Kakeshita, MRS Bull. **27**, 91 (2002).

[2] J. Mohd Jani, M. Leary, A. Subic, and M. A. Gibson, Mater. Design (1980-2015) **56**, 1078 (2014).

[3] P. S. Lobo, J. Almeida, and L. Guerreiro, Proc. Eng. **114**, 776 (2015).

[4] J. A. Shaw and S. Kyriakides, J. Mech. Phys. Solids **43**, 1243 (1995).

[5] T. Duerig, in *Titanium in Medical and Dental Applications*, edited by F. H. Froes and M. Qian, Woodhead Publishing Series in Biomaterials (Woodhead Publishing, Duxford, 2018), pp. 555–570.

[6] O. Benafan, M. R. Moholt, M. Bass, J. H. Mabe, D. E. Nicholson, and F. T. Calkins, Shape Mem. Superelasticity **5**, 415 (2019).

[7] J. Ma, I. Karaman, and R. D. Noebe, Int. Mater. Rev. **55**, 257 (2010).

[8] T. Fukuda, T. Saburi, T. Chihara, and Y. Tsuzuki, Mater. Trans., JIM **36**, 1244 (1995).

[9] T. H. Nam, T. Saburi, Y. Nakata, and K. Shimizu, Mater. Trans., JIM **31**, 1050 (1990).

[10] R. Zarnetta, R. Takahashi, M. L. Young, A. Savan, Y. Furuya, S. Thienhaus, B. Maaß, M. Rahim, J. Frenzel, H. Brunken, Y. S. Chu, V. Srivastava, R. D. James, I. Takeuchi, G. Eggeler, and A. Ludwig, Adv. Funct. Mater. **20**, 1917 (2010).

[11] A. N. Bucsek, G. A. Hudish, G. S. Bigelow, R. D. Noebe, and A. P. Stebner, Shape Mem. Superelasticity **2**, 62 (2016).

[12] O. Benafan, A. Garg, R. Noebe, G. Bigelow, S. Padula, D. Gaydosh, N. Schell, J. Mabe, and R. Vaidyanathan, Intermetallics **50**, 94 (2014).

[13] S. Liu, B. B. Kappes, B. Amin-ahmadi, O. Benafan, X. Zhang, and A. P. Stebner, Appl. Mater. Today **22**, 100898 (2021).

[14] W.-C. Kim, K.-R. Lim, W.-T. Kim, E.-S. Park, and D.-H. Kim, Prog. Mater. Sci. **123**, 100855 (2022).

[15] X. Huang, G. J. Ackland, and K. M. Rabe, Nat. Mater. **2**, 307 (2003).

[16] C. Gong, Y. Li, Y. Wang, and D. Yang, Modell. Simul. Mater. Sci. Eng. **14**, 33 (2006).

[17] N. Hatcher, O. Y. Kontsevoi, and A. J. Freeman, Phys. Rev. B **79**, 020202(R) (2009).

[18] N. Hatcher, O. Y. Kontsevoi, and A. J. Freeman, Phys. Rev. B **80**, 144203 (2009).

[19] K. Guda Vishnu and A. Strachan, Acta Mater. **58**, 745 (2010).

[20] N. A. Zarkevich and D. D. Johnson, Phys. Rev. Lett. **113**, 265701 (2014).

[21] J. B. Haskins, A. E. Thompson, and J. W. Lawson, Phys. Rev. B **94**, 214110 (2016).

[22] J. B. Haskins and J. W. Lawson, J. Appl. Phys. **121**, 205103 (2017).

[23] J. B. Haskins, H. Malmir, S. J. Honrao, L. A. Sandoval, and J. W. Lawson, Acta Mater. **212**, 116872 (2021).

[24] W.-S. Ko, Scr. Mater. **154**, 134 (2018).

[25] S. Kadkhodaei and A. van de Walle, Acta Mater. **147**, 296 (2018).

[26] P. Kumar and U. V. Waghmare, Materialia **9**, 100602 (2020).

[27] G. Eggeler, *Material Science and Engineering of NiTi Shape Memory Alloys: Fundamentals, Microstructure, Processing and Applications*, 1st ed. (Wiley-VCH, Weinheim, 2020).

[28] G. M. Michal and R. Sinclair, Acta Crystallogr., Sect. B **37**, 1803 (1981).

[29] W. Buhrer, R. Gotthardt, A. Kulik, O. Mercier, and F. Staub, J. Phys. F: Met. Phys. **13**, L77 (1983).

[30] R. R. Pezarini, H. S. Bernabé, F. Sato, L. C. Malacarne, N. G. C. Astrath, J. H. Rohling, A. N. Medina, R. D. dos Reis, and F. C. G. Gandra, Mater. Res. Express **1**, 026502 (2014).

[31] V. Shastry, V. Divya, M. Azeem, A. Paul, D. Dye, and U. Ramamurty, Acta Mater. **61**, 5735 (2013).

[32] W. Cai and K. Otsuka, J. Mater. Sci. Technol. **17**, 359 (2001).

[33] J. Khalil-Allafi and B. Amin-Ahmadi, J. Alloys Compd. **487**, 363 (2009).

[34] S. Prokoshkin, A. Korotitskiy, V. Brailovski, S. Turenne, I. Khmelevskaya, and I. Trubitsyna, Acta Mater. **52**, 4479 (2004).

[35] S. Miyazaki and K. Otsuka, Metall. Trans. A **17**, 53 (1986).

[36] K. Parlinski and M. Parlinska-Wojtan, Phys. Rev. B **66**, 064307 (2002).

[37] X. Zhang and H. Sehitoglu, Mater. Sci. Eng., A **374**, 292 (2004).

[38] X. Zhang, B. Grabowski, F. Körmann, C. Freysoldt, and J. Neugebauer, Phys. Rev. B **95**, 165126 (2017).

[39] See Supplemental Material at http://link.aps.org/supplemental/10.1103/PhysRevB.106.L140102 for the convergence test of computing the electronic free energy; the calculated data for structural parameters, and atomic coordinates; and the detailed description of computational procedures to obtain Gibbs free energy.

[40] G. Kresse and J. Hafner, Phys. Rev. B **47**, 558 (1993).

[41] G. Kresse and J. Hafner, Phys. Rev. B **49**, 14251 (1994).

[42] G. Kresse and J. Furthmüller, Comput. Mater. Sci. **6**, 15 (1996).

[43] G. Kresse and J. Furthmüller, Phys. Rev. B **54**, 11169 (1996).

[44] B. Grabowski, L. Ismer, T. Hickel, and J. Neugebauer, Phys. Rev. B **79**, 134106 (2009).

[45] J. P. Perdew, K. Burke, and M. Ernzerhof, Phys. Rev. Lett. **77**, 3865 (1996).

[46] P. E. Blöchl, Phys. Rev. B **50**, 17953 (1994).

[47] G. Kresse and D. Joubert, Phys. Rev. B **59**, 1758 (1999).

[48] A. Togo and I. Tanaka, Scr. Mater. **108**, 1 (2015).

[49] X. Huang, C. Bungaro, V. Godlevsky, and K. M. Rabe, Phys. Rev. B **65**, 014108 (2001).

[50] O. Hellman, I. A. Abrikosov, and S. I. Simak, Phys. Rev. B **84**, 180301(R) (2011).

[51] O. Hellman, P. Steneteg, I. A. Abrikosov, and S. I. Simak, Phys. Rev. B **87**, 104111 (2013).

[52] F. Falk, Acta Metall. **28**, 1773 (1980).